In Situ Transmission Electron Microscopy of Temperature-dependent Carbon Nanofiber and Carbon Nanotube Growth from Ethanol Vapor

Myeonggi Choe[1,2,‡], *Handolsam Chung*[1,2,‡], *Wonjun Kim*[1,2], *Younggeun Jang*[1,2], *Zhaoying Wang*[1,2], *and Zonghoon Lee*[1,2,*]

[1]Center for Multidimensional Carbon Materials, Institute for Basic Science, Ulsan 44919, South Korea

[2]Department of Materials Science and Engineering, Ulsan National Institute of Science and Technology (UNIST), Ulsan 44919, South Korea

‡These authors contributed equally: Myeonggi Choe and Handolsam Chung

*Corresponding author: zhlee@unist.ac.kr (Zonghoon Lee)

KEYWORDS: carbon nanofiber, carbon nanotube, active state, activation energy, growth mechanism, ethanol vapor, *in situ* TEM

Abstract

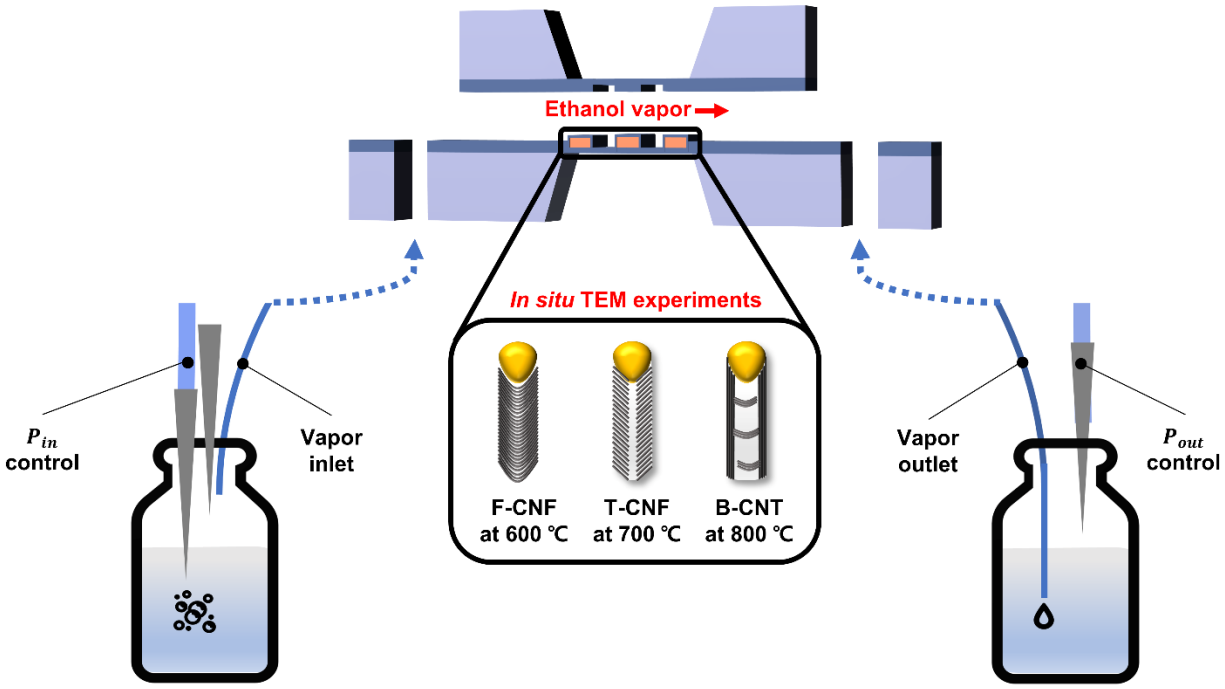

We report the *in situ* transmission electron microscopy (TEM) experiments to directly observe Ni catalysed CNFs/CNTs growth from alcohol precursor at near atmospheric pressure using a homebuilt bubbler system for the introduction of ethanol vapor. Using real time imaging, we revealed the active state of the Ni catalyst during the temperature-dependent CNFs/CNTs growth (600–800 °C). We observed the formation of CNFs starting from 600 °C and CNTs were formed at higher temperatures. The lattice parameter measurements pointed to an expansion of the Ni lattice as the temperature was increased, which we attribute to increased carbon solubility. The as-grown CNFs and CNTs were further characterized by XPS, Raman spectroscopy, and EELS, that allowed to have a highly reliable overall view of the structure changes with temperature. Results revealed that the change in structure with temperature was caused by the combined effects of increased carbon solubility and graphitization of the walls of the growing nanostructure. This increased carbon solubility in turn affected carbon diffusion and could be the reason for the change

in structure from CNF to CNT at high temperature. We also successfully identified the transition from tip-growth to base-growth in a CNT at 800 °C.

Introduction

Due to their extraordinary physical properties and chemical stability, carbon nanofibers (CNFs) and carbon nanotubes (CNTs) find applications in many areas including energy storage, wearable electronics, thermal interfaces, chemical sensors and photonics, among others.[1-3] Nevertheless, it is generally accepted that a precise control of their structure at the nano and micro level is indispensable to enable these applications. Among the different approaches adopted in CNF and CNT synthesis, chemical vapor deposition (CVD) involving the catalytic decomposition of carbonaceous precursors at temperatures in the range 600–1000 °C, is the most widely used, since it allows better control of structure and is scalable in addition to being a low cost process with high yield. Because of the special relationship between the structure and the versatile properties of the nanostructures formed, much research has been dedicated to understanding the growth mechanism of CNFs/CNTs formation by CVD.[4-6]

Among the different experimental variables in the CVD synthesis of CNFs/CNTs, such as temperature, pressure, and reactant gas concentration,[5, 7-9] the growth temperature is the most important parameter that crucially determines the structure of the product obtained, since the state of the catalyst is temperature dependent.[10-15] The growth temperature can control the degree of internal carbon diffusion by changing the amount of dissolved carbon.[16] Furthermore, higher growth temperatures usually led to improved crystallinity of the graphitic walls of CNT.[12] Despite significant progress in process development, currently, an indepth understanding of the effect of

temperature on the actual growth process is still not achieved, due to missing information on non equilibrium phenomena occurring at high temperature in the gas-solid reaction.

In this regard, *in situ* characterization techniques have provided valuable information on reaction mechanisms and intermediates. With the help of *in situ* X-ray diffraction (XRD),[17, 18] *in situ* X-ray photoelectron spectroscopy (XPS),[19-21] and *in situ* Raman spectroscopy[22-24] important insights have been obtained into the state of the catalyst particles and their role in CNF and CNT growth mechanisms at different temperatures. *In situ* XRD experiments confirmed that during CNT growth, a transition from pure Ni metal to the carbide phase occurs due to the increased amount of dissolved carbon.[18] Using *in situ* XPS analysis, it was possible to monitor the increase in Ni carbide fraction during the growth of a CNF at 700 °C.[19] Similarly, CNT growth rate and lifetime were tracked by following the change in G band fraction with temperature using *in situ* Raman spectroscopy.[22] However, these *in situ* techniques do not allow to simultaneously describe the dynamic changes in both structure and bonding of the active phase, and moreover, they provide spatially averaged information from a relatively large area.

In this context, *in situ* transmission electron microscopy (TEM) offers atomic- and nanoscale information on the physical and chemical states of individual catalytic particles through imaging and spectroscopy from which, important clues to the reaction mechanisms under different growth conditions can be obtained.[25-27] Using *in situ* TEM, it has been possible to determine the active state of catalyst particles, which when combined with favored carbon diffusion pathways derived from density functional theory (DFT) calculations, can provide a holistic view of the reaction mechanism.[8] Wang *et al.* reported that the active phase of the Co catalyst particle during the multiwall CNT growth is Co_3C and proposed that the main diffusion pathway is that between the catalyst surface and the graphitic wall.[28] Fan *et al.* reported that the active phase of a Ni–Co binary

alloy remains a pure metal during CNF growth and that the bulk diffusion is energetically more favorable than interface diffusion.[29] However, these previous *in situ* TEM studies on CNF and CNT growth used gaseous hydrocarbons as carbon precursors, while alcohol carbon sources, which have recently gained great attention due to their high yields, have so far not been studied.

Currently, alcohols (mainly ethanol) are the most used carbon precursors for large scale CNF and CNT growth, both due to economic and ecological concerns. Water molecules and hydroxyl radicals generated from the decomposition of alcohols act as etchant to prevent amorphous carbon formation due to which, the yield of reaction and catalyst lifetime can be significantly increased.[1, 5, 30] However, introducing a liquid vapor into an *in situ* TEM system with closed cell could be complicated by re-condensation of the vapor, which blocks the gas flow due to the limited available space at the reaction site and the ultra narrow diameter of the supply lines, in addition to the danger of contaminating supply lines, as a result of which, there are only rare studies on using ethanol vapor in an *in situ* TEM system.[31, 32] Thus, to the best of our knowledge, there are no reported *in situ* TEM studies on CNF and CNT growth using alcohol as the carbon source at near atmospheric pressure using a closed cell.

In this work, we report *in situ* TEM studies to elucidate the effect of temperature on the growth of CNFs and CNTs with Ni catalyst and ethanol as the carbon source at near atmospheric pressure. Our homebuilt bubbler system allowed to precisely flow ethanol vapor into a micro-electro-mechanical system (MEMS) based closed cell system in a controlled way while maintaining near atmospheric pressure conditions. Using this system, we successfully monitored the growth of CNFs and CNTs from alcohol precursor on a Ni catalyst at different temperatures. We performed *in situ* analysis on growing CNFs/CNTs at three different temperatures (600 °C, 700 °C, and 800 °C) to study the structure changes in real time. To gain a deeper understanding of the growth

mechanism in a real growth environment, we also conducted *ex situ* characterization (post-analysis) on the CNFs/CNTs that were grown using the same system and conditions for the comparison. Selected area electron diffraction (SAED) patterns were analyzed both under *in situ* and *ex situ* conditions to understand the active state during growth. Complementary spectroscopic techniques including XPS, Raman spectroscopy, and *in situ* and *ex situ* electron energy loss spectroscopy (EELS) allowed to get detailed information on the obtained structures. Combining *in situ* results with *ex situ* techniques on the same sample allowed to quantitatively estimate the increase in carbon solubility and the crystallinity of the walls (sp^2 carbon fraction and I_{D1}/I_G ratios) with growth temperature in a reliable manner. We surmise that the increased carbon solubility modified carbon diffusion and crucially affected the structure of the growing nanofiber or nanotube.

Results/Discussion

CNF and CNT synthesis with ethanol vapor

Our *in situ* TEM experiments on CNF and CNT growth with ethanol vapor as the carbon source were conducted using a MEMS-based closed cell connected to a homebuilt bubbler system. We modified the commercial gas distributer system from DENSsolutions to supply ethanol in the vapor state by replacing the gas supply lines with our homebuilt bubbler system. Two vials with pumps were connected to the gas inlet (P_{in}) and outlet (P_{out}) lines, which allowed to precisely control the pressure and flow rate at the reaction site (P_{r} and F_{r}) in the closed cell (Figure 1a and Video S1). The working pressure and flow rate at the reaction site were calculated as described in SI and Tables S1–2.[33] Thus, our bubbler system enabled as good control of both pressure and flow rate as commercially available gas flow systems (Figure S1), which allowed to grow CNFs and CNTs at different temperatures with high reproducibility. To precisely understand the effect of

temperature on growth, we fixed the internal pressure at the reaction site at near atmospheric pressure and observed the growth and changes in carbon structure as the temperature was increased. Ni nanoparticles were used as the catalyst in view of their high catalytic activity,[5, 34-36] and ethanol, being weakly oxidizing, was selected as the carbon source to obtain high growth yield.[37-41]

We identified the formation of a carbonaceous structure upon heating first at 540 °C, and noticeable structural changes were confirmed in the temperature range of 600–800 °C (Figure 1b). A fishbone-type CNF (F-CNF) was formed at a relatively low temperature of 600 °C and this structure changed to a tubular CNF (T-CNF) at 700 °C. At 800 °C, the main structure grown was a bamboo-type CNT (B-CNT).[13] All the three tubular structures were formed by tip-growth mode, but a change in the growth mechanism from the tip- to base-growth also occurred occasionally at 800 °C, ending in a multiwalled CNT (M-CNT). In tip-growth mode, the carbon source decomposes on the exposed surface of the catalyst particle and the carbon atoms diffuse towards the rear side of the catalyst (in proximity to the substrate). The carbon atoms precipitate to form graphitic walls along a direction opposite to the growth direction. A closer look at the images in Figure 1b reveals the presence of graphitic walls on F-CNF grown by precipitation of carbon atoms at the rear surface (surface opposite to the exposed surface) of the catalyst and stacked almost perpendicularly to the growth direction. T-CNF also has graphitic walls similar to F-CNF, grown by precipitation on the rear surface, but these did not completely cover the particle but left a hollow column as shown in the schematic. B-CNT shows graphitic walls along the growth direction with internal closures (knots) that separate the columns.

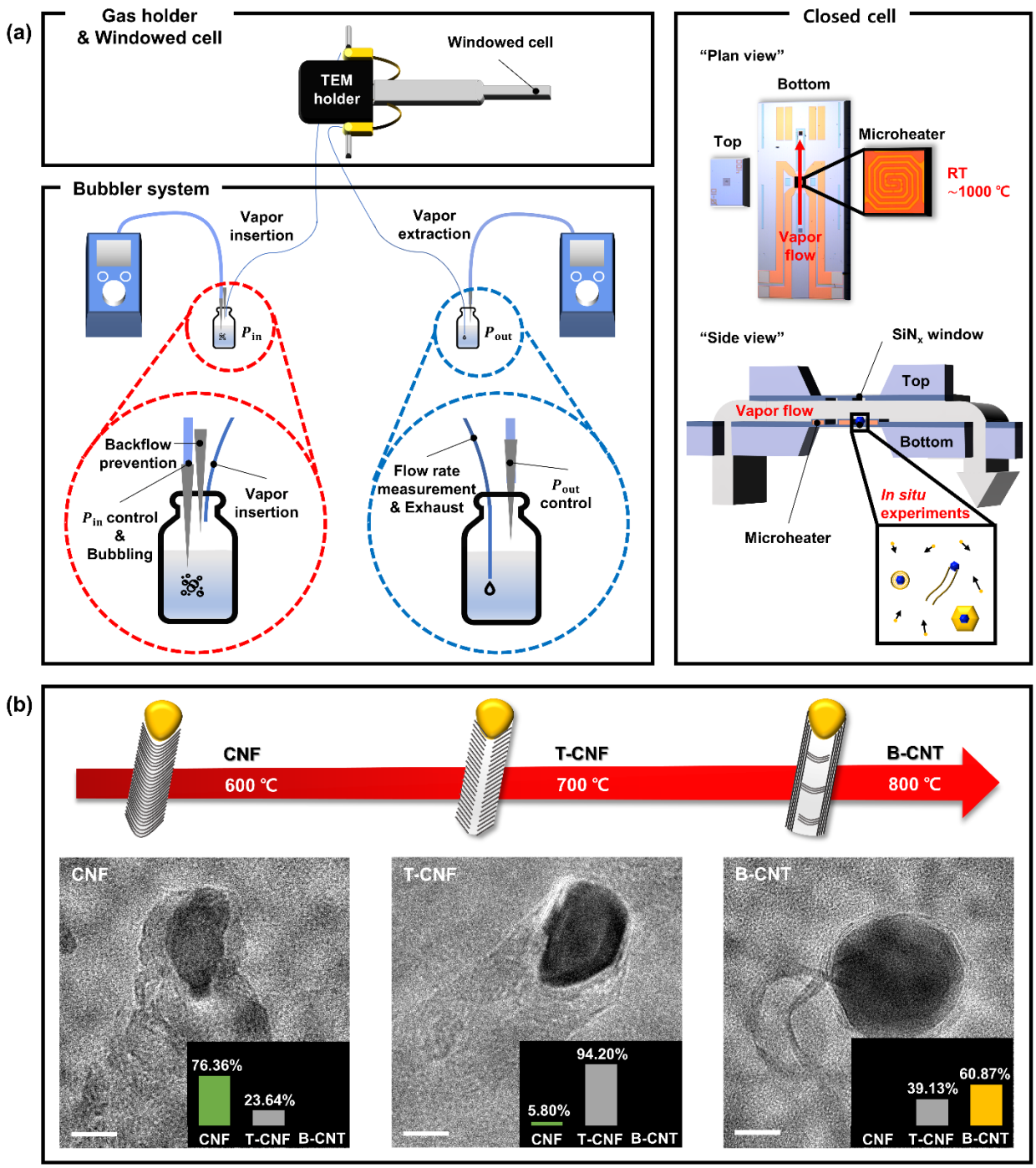

Figure 1. *In situ* TEM experiments where liquid vapor was introduced into a closed cell using the homebuilt bubbler system. (a) Schematic of the devised bubbler system and the closed cell. (b) Temperature-dependent growth of CNF and CNT with ethanol as carbon source. Scale bars are 10 nm.

State of the catalyst during the growth

The structure of the growing CNF/CNT is intimately connected to the state of the catalyst. During growth, the amount of dissolved carbon inside the catalyst particle impacts the degree of carbon diffusion and critically affects the structure of the growing CNFs/CNTs.[9, 16, 42-46] We imaged the active phases of the Ni catalyst during CNF and CNT growth in the temperature range of 600–800 °C. TEM images show that the overall structure remained similar to that of pure Ni (Figure S2), but measurement of SAED patterns with rotational average intensity profiles revealed a slight increase in lattice constant indicating that the Ni crystal expanded during the growth (Figure S3 and Table S3). Although we attempted atomic-resolution imaging to accurately determine the state of the catalyst during the reaction, the high electron beam dose (1380 $e^{-1}/Å^2 \cdot s$) under high magnification perturbed the growth (Figure S2 and Videos S2, S3). Due to the defects induced by the electron beam irradiation, the graphitic walls formed under the high electron beam dose resulted in helical-like growth (Video S2) or sometimes just collapsed without undergoing sustained growth (Video S3). In view of this electron beam effect, we decided to use data taken under relatively lower electron beam dose conditions (7.92 $e^{-1}/Å^2 \cdot s$) and found that analyzing SAED patterns was a more appropriate method than atomic-resolution imaging to understand the exact state of the catalyst during the growth.

To determine the change in average lattice constant with temperature, we averaged SAED patterns with rotational intensity profiles from Figure S3 and Table S3 (Figure 2 and Table S4). We note here that, due to dissolved carbon in the catalyst and the formation of carbonaceous species by the decomposition of ethanol vapor, our *in situ* TEM images appear more blurry (Figure 2a–c) compared to the those obtained in post-analysis of the grown carbon structures (Figure 2d–f).[47] A clear increase in the average lattice constant of the catalyst was observed in our *in situ*

experiment (Table S4). The lattice constants at 600 ℃, 700 ℃, and 800 ℃ were 3.6079 ± 0.0026 Å, 3.6226 ± 0.0043 Å, and 3.7187 ± 0.0052 Å (Figure 2a–c and Table S4). Comparison of our experimental results with reference thermal expansion data confirmed that the lattice expansion was not due to thermal expansion but was caused by dissolved carbon (Figure S4).[48, 49] We then calculated the carbon concentrations corresponding to this lattice expansion at 600 ℃ and 800 ℃ to be ~7.56 at.% and ~20.38 at.%, respectively (Figure S5),[18] which incidentally, are much higher than the carbon solubility in bulk Ni.[50, 51] On the other hand, post-analysis of the grown structures (Figure 2d–f and Table S4), indicated only a very slight lattice expansion and the corresponding carbon concentrations at 600 ℃ and 800 ℃ were ~0.50 at.% and s ~4.22 at.%, respectively. We attribute this difference to additional growth during cooling after cutting off the carbon source supply, during which process, a certain amount of dissolved carbon could be consumed by forming additional graphitic walls.

The difference in lattice constant changes between *in situ* results and *ex situ* analysis provides us a good tool to understand the structural changes occurring during the growth, and allows to better understand the growth mechanism. Previous studies have reported that dissolved carbon in a Ni catalyst can weaken the interaction between the graphene and the surface of the catalyst,[52] and hence the increased carbon concentration at higher temperatures could lead to a detachment of the graphitic wall with a lower adhesion force. This behavior is expected in our experiments as well, and could be reason for the observed structure changes

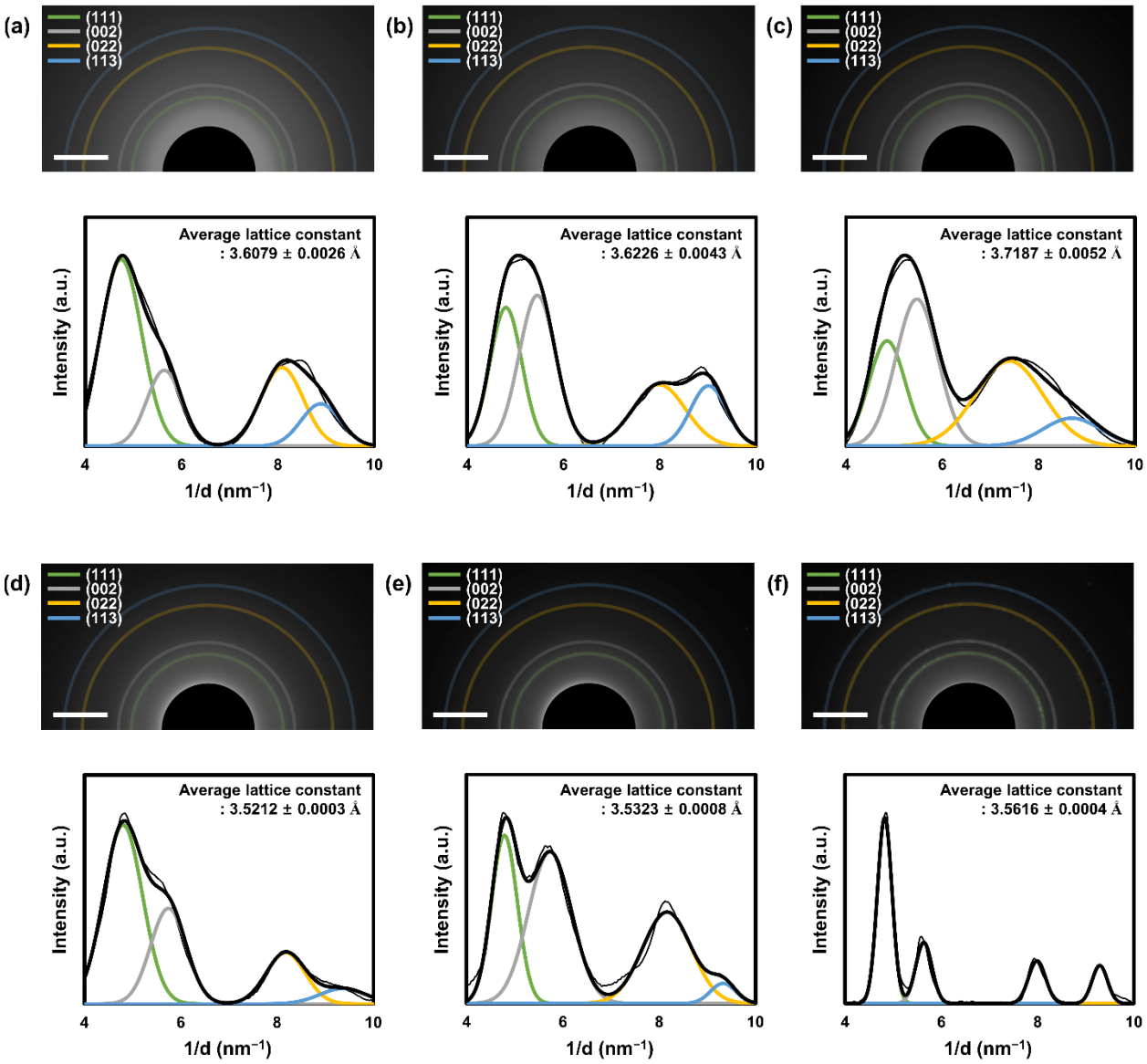

Figure 2. Averaged SAED patterns with the rotational average intensity profiles showing change in d-spacing with growth temperature. (a–c) Diffraction patterns during the reaction at (a) 600 °C, (b) 700 °C, and (c) 800 °C. (d–f) Diffraction patterns from *ex situ* analysis of grown structure at (d) 600 °C, (e) 700 °C, and (f) 800 °C. Scale bars are 2.5 nm^{-1}.

Temperature-dependent carbon bonding state change.

The mechanical, electrical, and optical properties of CNF and CNT can be modulated by changing the ratio of sp^2 to sp^3 bonds, which in turn, is a measure of the degree of graphitization.[53, 54] During *in situ* TEM experiments, we also performed electron energy-loss spectroscopy (EELS) analysis of the sample to reveal the changes in the bonding state of carbon at different temperatures. These effects were also investigated using complementary spectroscopic studies, such as XPS and Raman spectroscopy, so as to minimize possible systematic errors and get a clear picture of how the temperature affects the carbon bonding state. Additionally, to compare the results obtained from the same structures and verify the difference between *in situ* and post-analysis results, the EELS measurement was carried out both *in situ* and *ex situ*.

In the case of EELS, the density of anti-bonding π^* and σ^*states can be used to calculate the fraction sp^2 bonds.[55-57] To accurately quantify this fraction, we adopted the "Five Gaussian Peaks Method" by Mironov *et al*.[58] This method was developed by adding two additional Gaussian peaks to the "Three Gaussian Peaks" method proposed by Zhang *et al*.[55] Using this method, we estimated the sp^2 fraction at each temperature (Figure 3a,b), and the parameters used for fitting are listed in SI and Table S5. The actual sp^2 fraction can be calculated by comparing the peak intensities of π^* and σ^* to those of a 100% sp^2-hybridized material as shown in SI.[57] Our results show that the sp^2 fraction tends to increase with temperature. Though the sp^2 fraction values obtained from the post-analysis were slightly higher than those from *in situ* analysis, which might be caused by additional crystallization during cooling, a similar overall trend was observed in both cases.

XPS can also be used to estimate the sp^2 and sp^3 fractions. However, an interpretation of XPS C1s could be difficult in the presence of disordered carbons and carbons bonded to other species (such as oxygen) due to binding energy shifts associated with various heteroatoms. Smith *et al.*

proposed a good alternative method based on the 7 peak C1s deconvolution (3 C–C peaks, 3 oxygenated peaks, and π–π^* transition peak).[59] We applied this deconvolution method to our results to identify the sp^2 and sp^3 fractions at each temperature (Figure 3c); the parameters used for fitting are listed in SI and Table S6. The observed trend in sp^2 fraction at different temperatures obtained from XPS is in good agreement with our EELS analysis (Figure 3e), confirming increase in sp^2 bonds fraction with temperature.[60-62] We confirmed this result by performing additional EELS deconvolution using the "Sum of Decaying Gaussian Peaks Method", where we assigned the asymmetric C=C π^* peak (we chose this peak because of its asymmetric nature; SI, Figure S6 and Table S7).[63] The calculated sp^2 fractions using this method were a little higher but still in good agreement with the trend shown in Figure 3e.

The structures of CNF and CNT were further analyzed using Raman spectroscopy.[64, 65] Though Raman analysis cannot directly give information on sp^2 and sp^3 fractions, the ratio of the intensities of the D1 and the G band is related to impurities, defects, and disorder in CNF and CNT.[66, 67] Sadezky *et al.* proposed a combination of four Lorentzian peaks (G, D1, D2, and D4) and one Gaussian peak (D3) for the Raman spectral investigation of carbon materials.[68] We used this deconvolution method (SI, Figure 3d and Table S8) to calculate the I_{D1}/I_G ratios. The I_{D1}/I_G ratio and the sp^2/sp^3 ratio, both indicative of the degree of graphitization of carbon networks, are known to correlate with each other.[69-71] The measured I_{D1}/I_G ratio decreases with increasing temperature, implying increased graphitization with temperature, which correlates with the increasing sp^2/sp^3 ratio obtained from XPS analysis (Figure 3f). Thus, results from complementary spectroscopic studies show consistency over EELS, XPS, and Raman spectroscopy.

To sum up the overall spectroscopic analysis results, the effect of temperature on the degree of graphitization was verified by determining the sp^2 fraction or the sp^2/sp^3 ratio change, and EELS

analysis confirmed that there was no significant difference in temperature effect between *in situ* and post-analysis results.

Jacobson *et al.* reported that thermal healing of disorders and defects in graphene on a Ni surface requires temperatures greater than 700 °C[72] and Fan *et al.* reported that the defect density in a graphitic wall growing on a catalyst particle surface is directly related to the adhesion force between them.[29] Consequently, a change in the sp^2 fraction (or defect density) with temperature could induce a change of structure.

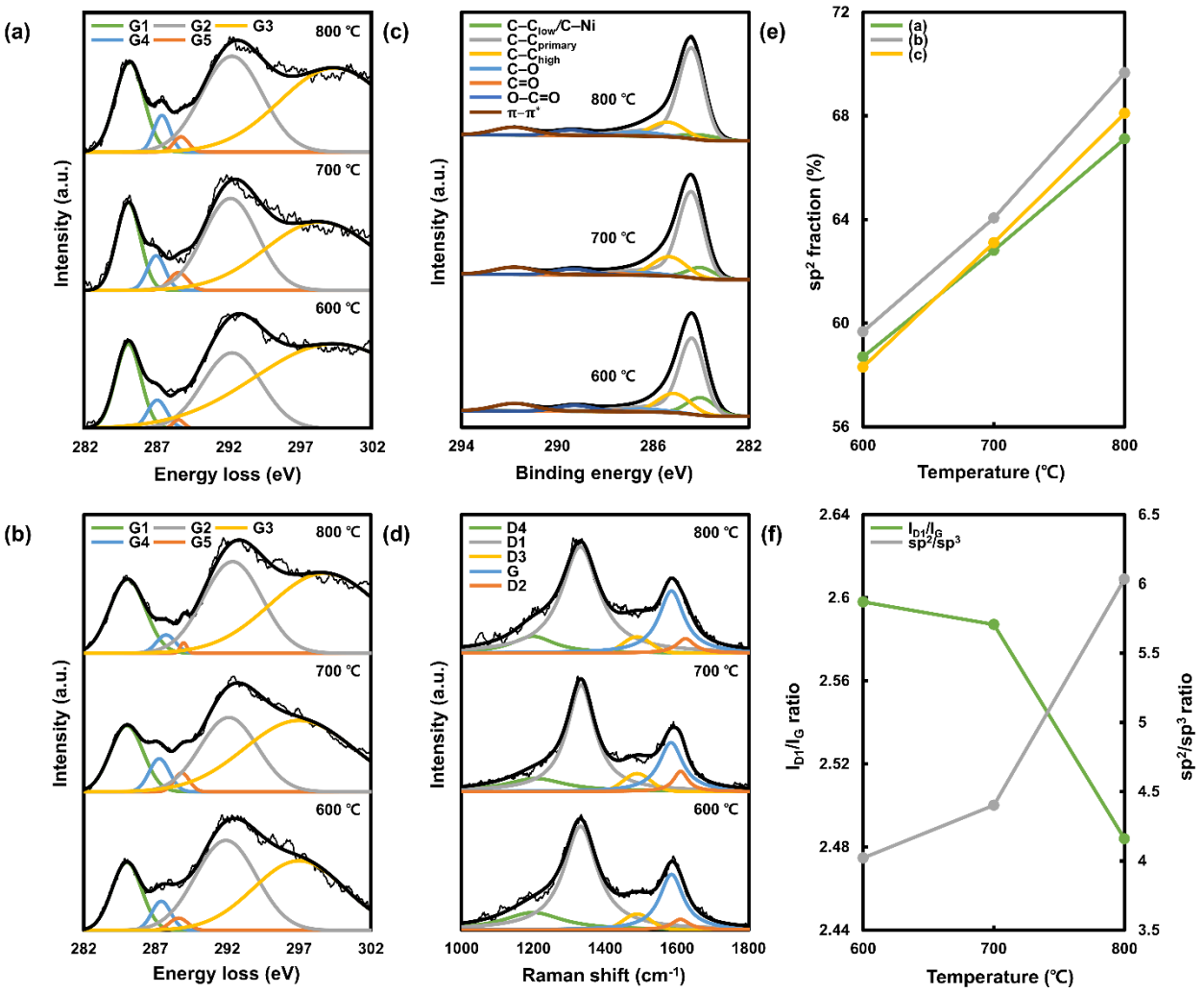

Figure 3. Complementary spectroscopic analysis to understand the temperature-dependent growth mechanism. EELS obtained through (a) *in situ* analysis during the growth and (b) *ex situ* analysis on the grown CNF and CNT. (c) XPS and (d) Raman spectra obtained from *ex situ* analysis. (e) The comparison of EELS and XPS showing the relative sp^2 fractioin change with the temperature. (f) The comparison of I_{D1}/I_G from Raman spectroscopy and sp^2/sp^3 from XPS with temperature.

Temperature-dependent growth kinetics

To study the temperature-dependent growth kinetics, the trajectories of CNF and CNT were monitored, and their growth rates were measured by dynamically observing their growth (Figure 4a–c). We focused on CNFs and CNTs growing by tip-growth mode and a statistical analysis was performed on 70 cases at 600 °C, 101 cases at 700 °C, and 68 cases at 800 °C. Results show that growth rates are affected by both particle size and temperature (Figure S7).[12, 73-76] The growth rate was faster as the catalyst particle size decreased and also increased with temperature. Therefore, we distributed the particles into three groups of similar sizes (18–20 nm, 21–23 nm, and 24–26 nm), to eliminate the effect of particle size when studying temperature dependence. Figure 4d–f shows the average values of the selected results, and the whole data with individual growth rates measurements are in given in Figures S8, S9 and Videos S4–6.

Estimating the activation energies (E_a) from the growth rates of CNF and CNT gives important clues to understanding the carbon diffusion pathway during growth. Hence, we calculated the activation energies of CNF and CNT growth using the Arrhenius equation. So far, studies on activation energies for CNF and CNT formation are usually derived based on the CVD-grown end product. These calculated values could be erroneous since they include the nucleation and termination steps in addition to the actual growth step. Therefore, the direct observation of CNF and CNT during the growth stage gives us a better picture of the actual growth process and allows to calculate the corresponding activation energies.

As shown in Figure 4g–i, in the temperature range 600–700 °C, there was no significant difference in activation energies for the three size groups. However, in the 700−800 °C temperature range, the E_a values obtained for the 18–20 nm group were slightly higher than for the other two size groups. We attribute this difference to the hampered growth rate for low particle sizes at high

temperature, caused by the relatively large amount of dissolved carbon. Nevertheless, it is seen that the overall trends with temperature are similar for the three size groups. At temperature ranges of 600–700 °C and 700–800 °C, the average activation energies for CNFs and CNTs were 0.76 eV and 0.93 eV for the three different groups. The increase in activation energy from CNF to CNT indicates either a change in the state of the catalyst or that the diffusion of carbon was affected by the increased amount of interstitially dissolved carbon, as explained in Figures 2, S5 and Table S4.

The free carbon atoms generated from a decomposed carbon source on the surface of the catalyst can diffuse in several ways to form graphitic walls, including surface diffusion (diffusion along the surface), bulk diffusion (diffusion through the particle), subsurface diffusion (diffusion from the surface to the subsurface), and subsurface bulk diffusion (diffusion along the layer just below the surface). The theoretical values of activation energies derived from DFT calculations for surface diffusion, bulk diffusion, subsurface diffusion, and subsurface bulk diffusion are 0.19–0.29 eV (θ = 0.0625–0.11 ML), 1.62–1.83 eV, 0.55–0.76 eV (θ = 0.0625–0.11 ML), and 0.86–1.16 eV (θ = 0.0625–0.11 ML),[18, 77] where a monolayer (ML) is defined by the atomic density on the Ni(111) surface, and θ is the surface coverage of carbon in the ML. Furthermore, after the formation of graphitic walls, we need to consider an additional diffusion pathway, which is the diffusion at the interface between the grown graphitic wall and the catalyst surface. The activation energies for this interface diffusion can be differentiated depending on whether the grown structure is a CNF or CNT. In the case of a CNF, the interface diffusion is energetically less favorable compared to bulk diffusion.[29] In contrast, for a CNT, the activation energy of interface diffusion is close to that of surface diffusion when the grown walls have zig-zag edges (when they have armchair edges, the activation energy for interface diffusion becomes higher than that of surface diffusion).[28] Comparing our derived activation energies with the theoretical values from DFT

calculations, we infer that subsurface bulk diffusion would be the rate-determining step for CNF and CNT growth in the temperature range of 600–800 °C.

Based on the above findings, looking at each growing structure in more detail, F-CNF at 600 °C could be formed by the simultaneous precipitation of carbon atoms at the rear surface of the catalyst by surface diffusion as well as by subsurface bulk diffusion. Because the surface diffusion would be energetically favorable, the subsurface bulk diffusion would be the rate-determining step during CNF formation. A similar approach could be applied to T-CNF grown at 700 °C. However, at higher temperatures, due to the increased amount of dissolved carbon, the subsurface bulk diffusion to the backside of the particle (side opposite to the growth direction) would be relatively difficult,[16] while the interface diffusion would be energetically unfavorable. Hence, a transition from F-CNF to T-CNF is likely to occur. B-CNT growth at 800 °C would be the result of different degrees of contribution from each of the diffusion pathways, which are surface-, interface-, and subsurface bulk diffusion. The main diffusion pathways for the growth of graphitic walls during CNT formation would be the energetically favorable surface diffusion and interface diffusion, and the overall growth would be determined by the subsurface bulk diffusion.

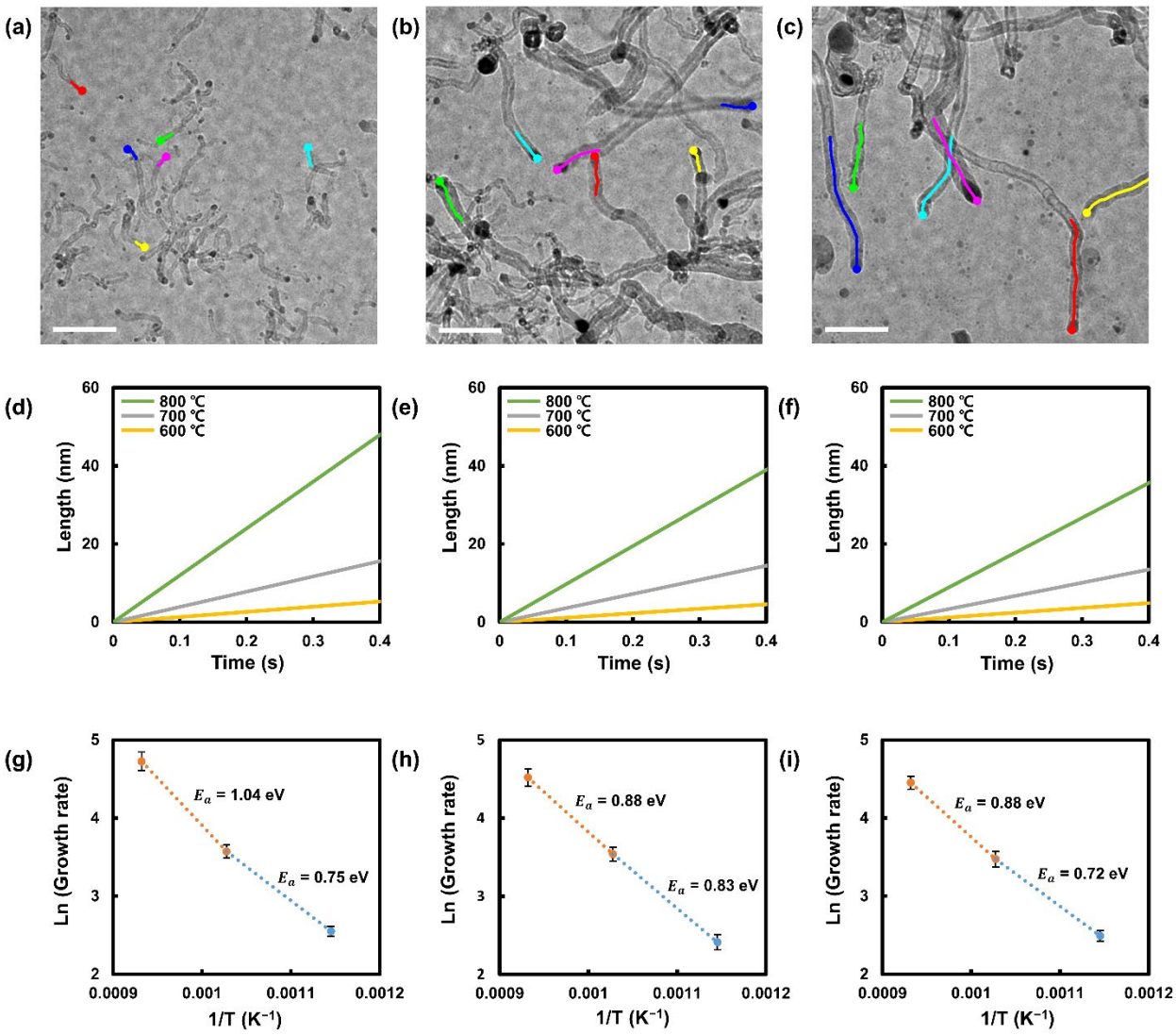

Figure 4. CNF and CNT growth kinetics from *in situ* TEM experiments. Representative images showing the growth trajectories at (a) 600 ℃, (b) 700 ℃, and (c) 800 ℃. Averaged growth lengths as a function of time for particle sizes in the range of (d) 18–20 nm (e) 21–23 nm, and (f) 24–26 nm. Arrhenius plots for the CNF and CNT growth rates with particle sizes in the ranges (g) 18–20 nm, (h) 21–23 nm, and (i) 24–26 nm. The blue and orange dotted lines correspond to the 600–700 ℃, and the 700–800 ℃ temperature ranges. Scale bars are 100 nm.

Tip- to base-growth mode change during the CNT growth.

At the temperature of 800 °C, in addition to B-CNT growing by tip-growth mode (Figure 5a), a CNT growing by base-growth mode was also observed (Figure 5b). This growing CNT formed a M-CNT in the shape of a hollow cylinder without having internal closures (knots) which are seen in the general bamboo-type structure. It is generally known that a transition to a base-growth can occur depending either on the particle size or on the catalyst-substrate interaction. However, in our experiment, this transition was seen in particles with sizes ~30 nm. Therefore, under our experimental conditions, we think that this transition could be due to increase in interaction energy with the substrate, since at these temperatures, the catalyst could be in a more molten-like state and the amount of dissolved carbon could be higher.[78]

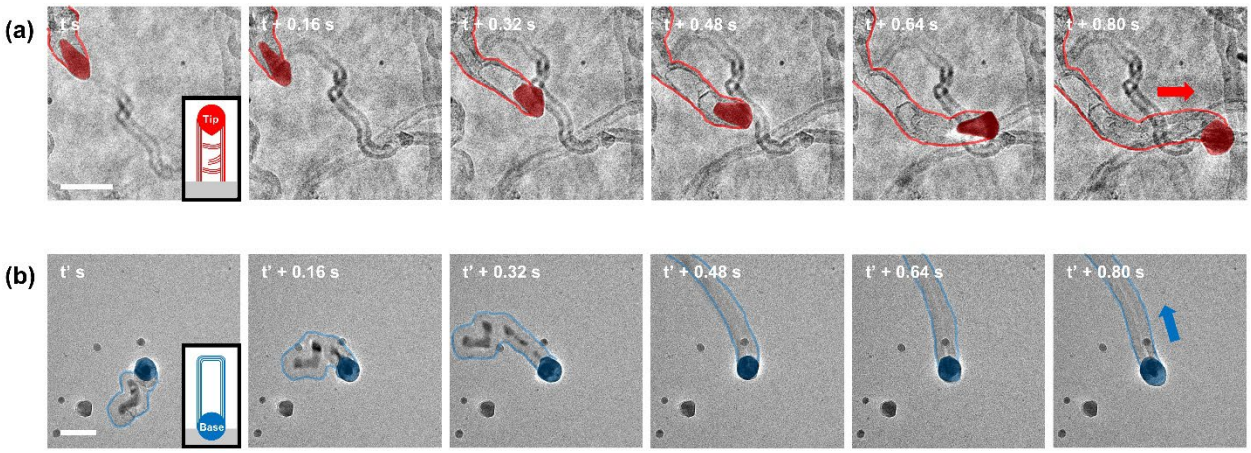

Figure 5. *In situ* TEM observation of the CNT tip- to base-growth mode change at 800 °C. Sequential TEM images showing (a) a B-CNT growing by tip-growth mode, and (b) M-CNT growth through base-growth mode. Scale bars are 50 nm.

Conclusion

We carried out *in situ* TEM experiments to dynamically observe the growth of CNF and CNT using the homebuilt bubbler system that allowed the controlled introduction of ethanol vapor. Direct atomic- and nanoscale imaging in combination with the complementary spectroscopic analyses revealed temperature-dependence of CNFs/CNTs growth (600–800 °C) at near atmospheric pressure; CNFs and CNTs were formed in the low and high temperature ranges, respectively. Statistical analysis of SAED patterns showed that the Ni lattice expanded, likely due to increased amount of dissolved carbon during the growth, which could reduce the adhesion force between the graphitic walls and the catalyst. EELS, XPS, and Raman spectroscopy revealed that the degree of graphitization increased with temperature, which would also contribute to lowering the adhesion force. These temperature effects may be the reason for the observed structural change from CNF to CNT with increase in temperature. Calculated activation energies from measured growth rates showed subsurface bulk diffusion to be the rate-determining step for CNF and CNT growth, which would be affected by the increased carbon concentration depending on the growth temperature. Our experiments also demonstrate that the catalyst state in the growth environment is significantly different from that determined after growth from post-analysis (due to the different amount of dissolve carbon), further highlighting the necessity for *in situ* characterization. Our findings thus contribute to improving our understanding on the growth mechanisms of CNF and CNT formation under diverse environments, going beyond the limitations of previous studies. A greater understanding of the growth mechanism is expected to enable better structure control and help in setting guidelines to obtain the most ideal structure for a specific application.

Methods/Experimental

Preparation of Ni catalyst

3 nm-thick Ni films were deposited onto the surface of closed cells (DENSsolutions gas heating chip) using an electron beam evaporator (WOOSUNG, WC-4000) under high vacuum conditions (~5×10^{-6} torr). The cells were chosen from the same batch to ensure reproducibility in repeated experiments. The Ni deposited closed cells were then loaded into the gas holder (DENSsolutions gas holder). The gas supply lines in the gas holder and in the homebuilt bubbler system were flushed by 4% H_2 in Ar gas for a short time to remove residual gases. The deposited catalyst on the chip was then annealed at 800 °C to form Ni nanoparticles.

In situ TEM experiments

A homebuilt bubbler system was used to control the pressure and the gas flow at the reaction site. *In situ* experiments were conducted on an aberration-corrected TEM (FEI, Titan^3 G2 60-300) operated at 200 kV. CNF and CNT growth studies were performed at 600, 700, and 800 °C, with a pressure of 728 mbar and a flow rate of 0.43 ± 0.0029 ml/min. The carrier gas (4% H_2 in Ar) was saturated with ethanol vapor by bubbling the gas through the inlet vial (theoretically 6.5% C_2H_6O in Ar at 22 °C), and was directly introduced into the closed cell. For growth kinetics study, sequential images were acquired using a Gatan camera (BM-Ultrascan) at time intervals of 0.16 s with an exposure time of 0.1 s, and the dose rate was 7.92 $e^{-1}/Å^2 \cdot s$, under which conditions the growth was not affected by the electron beam. For atomic-resolution imaging, the exposure time was 0.1 s and the dose rate was 1380 $e^{-1}/Å^2 \cdot s$; under these conditions, beam-induced artifacts were observed.

Complementary spectroscopic analysis

Complementary spectroscopic techniques were used to characterize the CNF and CNT obtained from *in situ* TEM experiments. EELS was recorded from the same TEM described above with a Gatan Quantum 965 dual EELS system in STEM mode. During the measurement, the energy dispersion was 0.025 eV/ch and the energy resolution was 1.0 eV under an acceleration voltage of 200 kV. XPS (Thermo Fisher Scientific, ESCALAB 250XI) was performed with monochromatic Al Kα radiation. XPS analysis area was set to 200 μm beam diameter and the step size was 0.1 eV with a base pressure of 1×10^{-10} torr during all measurements. Raman spectra were collected on a Raman Microscope system (WITec, alpha300S) equipped with 532, 633, and 785 nm lasers; in our measurements, we used the 633 nm laser to reduce plural scattering.

SAED pattern indexing

A 60 μm-size selected-area aperture was used to acquire the SAED patterns, and these were captured from six different positions at each condition. SAED patterns were analyzed using the DiffTools package for Digital Micrograph® software (industry standard software for TEM analysis). Rotationally averaged radial intensity profiles were obtained and the acquired profiles were automatically indexed using the top hat filter (THF) tool in the DiffTools to reduce measurement errors. The *d*-spacing value of each crystal plane was obtained through auto-indexing, and the *d* values were converted to lattice constants. From these data, the average lattice constant for the entire region was derived.

Calculation of activation energies during CNF and CNT growth

For calculating the energies of activation for CNF and CNT growth (Figure 4g–i), their growth rates were measured during the growth stage by successively capturing images (Figure S7 and Figure S8). The moving trajectories of each growing structure were tracked down manually using the Manual Tracking plugin in ImageJ software. Since the growth was accompanied by random orientation, the segments showing constant growth were measured. A sufficient number of growing structures were tracked down for statistical analysis to correctly estimate the effect of temperature on growth rate. The growth rate showed oscillatory behavior during the growth, as also reported in previous works.[27-29] The average growth rate with respect to temperature change was used for the calculation of activation energies. The activation energy (E_a) was calculated according to the modified Arrhenius equation.

$$\ln k = -\frac{E_a}{k_B T} + \ln A$$

Where, k is the growth rate, k_B is the Boltzmann constant, T is the absolute temperature, and A is the pre-exponential factor. The gradient from the plot of $\ln k$ versus T^{-1} was be used to determine the activation energy.

ASSOCIATED CONTENT

Supporting Information

Proof of system reliability for the homebuilt bubbler system; tables showing measured gas flow rate using the bubbler system; the active phase of the catalyst during the growth of CNF and CNT; SAED analysis; tables showing lattice constants from SAED patterns; the comparison of changes in lattice constant caused by thermal expansion and that due to amount of dissolved carbon; carbon concentration of the Ni particle; deconvolution of EELS spectra; tables showing the peak positions and parameters used for the deconvolution of EELS, XPS, and Raman spectra; size-dependent growth rate changes; temperature-dependent growth rate changes; distribution of growth rates according to the catalyst size and growth temperature ; calculation on the working pressure and flow rate; details of complementary spectroscopies (PDF)

Video S1: Homebuilt bubbler system (MP4)

Video S2: Helical-like growth due to defects induced by electron beam irradiation (MP4)

Video S3: Collapse of graphitic walls due to defects induced by electron beam irradiation (MP4)

Video S4: *In situ* growth experiment at 600 ℃ (MP4)

Video S5: *In situ* growth experiment at 700 ℃ (MP4)

Video S6: *In situ* growth experiment at 800 ℃ (MP4)

AUTHOR INFORMATION

Corresponding Author

Zonghoon Lee - Center for Multidimensional Carbon Materials, Institute for Basic Science, Ulsan 44919, South Korea; Department of Materials Science and Engineering, Ulsan National Institute of Science and Technology, Ulsan 44919, South Korea;

https://orcid.org/0000-0003-3246-4072; email: zhlee@unist.ac.kr

Authors

Myeonggi Choe - Center for Multidimensional Carbon Materials, Institute for Basic Science, Ulsan 44919, South Korea; Department of Materials Science and Engineering, Ulsan National Institute of Science and Technology, Ulsan 44919, South Korea

Handolsam Chung - Center for Multidimensional Carbon Materials, Institute for Basic Science, Ulsan 44919, South Korea; Department of Materials Science and Engineering, Ulsan National Institute of Science and Technology, Ulsan 44919, South Korea

Wonjun Kim - Center for Multidimensional Carbon Materials, Institute for Basic Science, Ulsan 44919, South Korea; Department of Materials Science and Engineering, Ulsan National Institute of Science and Technology, Ulsan 44919, South Korea

Younggeun Jang - Center for Multidimensional Carbon Materials, Institute for Basic Science, Ulsan 44919, South Korea; Department of Materials Science and Engineering, Ulsan National Institute of Science and Technology, Ulsan 44919, South Korea

Zhaoying Wang - Center for Multidimensional Carbon Materials, Institute for Basic Science, Ulsan 44919, South Korea; Department of Materials Science and Engineering, Ulsan National Institute of Science and Technology, Ulsan 44919, South Korea

Author Contributions

M.C. and H.C. contributed equally to this work. M.C. conceived the idea. M.C. and H.C. planned the research, carried out the in situ TEM experiments, performed data analysis, and wrote the manuscript. W.K. conducted the XPS and Raman spectroscopy measurements. Y.J. contributed to the sample preparation using the electron beam evaporator. Z.W. participated in discussions. Z.L. supervised the project and edited the manuscript. All authors approved the manuscript.

Notes

The authors declare no competing financial interest.

ACKNOWLEDGMENT

We appreciate valuable discussion with Professor Feng Ding. This work was supported by the Institute for Basic Science (IBS-R019-G1).

References

(1) Yang, F.; Wang, M.; Zhang, D.; Yang, J.; Zheng, M.; Li, Y. Chirality pure carbon nanotubes: Growth, sorting, and characterization. *Chem. Rev.* **2020**, *120* (5), 2693-2758.
(2) Rao, R.; Pint, C. L.; Islam, A. E.; Weatherup, R. S.; Hofmann, S.; Meshot, E. R.; Wu, F.; Zhou, C.; Dee, N.; Amama, P. B. Carbon nanotubes and related nanomaterials: critical advances and challenges for synthesis toward mainstream commercial applications. *ACS nano* **2018**, *12* (12), 11756-11784.
(3) De Volder, M. F.; Tawfick, S. H.; Baughman, R. H.; Hart, A. J. Carbon nanotubes: present and future commercial applications. *science* **2013**, *339* (6119), 535-539.
(4) Maruyama, T. Carbon nanotube growth mechanisms. In *Handbook of carbon nanotubes*, Abraham, J., Thomas, S., Kalarikkal, N. Eds.; Springer, 2022; pp 57-87.
(5) Jourdain, V.; Bichara, C. Current understanding of the growth of carbon nanotubes in catalytic chemical vapour deposition. *Carbon* **2013**, *58*, 2-39.
(6) Brukh, R.; Mitra, S. Mechanism of carbon nanotube growth by CVD. *Chem. Phys. Lett.* **2006**, *424* (1-3), 126-132.
(7) Kharlamova, M. V. Investigation of growth dynamics of carbon nanotubes. *Beilstein J. Nanotechnol.* **2017**, *8* (1), 826-856.
(8) Kumar, M. Carbon nanotube synthesis and growth mechanism. In *Carbon nanotubes-synthesis, characterization, applications*, Yellampalli, S. Ed.; InTech, 2011; pp 147-170.
(9) Moisala, A.; Nasibulin, A. G.; Kauppinen, E. I. The role of metal nanoparticles in the catalytic production of single-walled carbon nanotubes—a review. *J. Phys.: Condens. Matter* **2003**, *15* (42), S3011.
(10) Simon, A.; Seyring, M.; Kämnitz, S.; Richter, H.; Voigt, I.; Rettenmayr, M.; Ritter, U. Carbon nanotubes and carbon nanofibers fabricated on tubular porous Al2O3 substrates. *Carbon* **2015**, *90*, 25-33.
(11) Kang, J.; Li, J.; Du, X.; Shi, C.; Zhao, N.; Nash, P. Synthesis of carbon nanotubes and carbon onions by CVD using a Ni/Y catalyst supported on copper. *Mater. Sci. Eng., A* **2008**, *475* (1-2), 136-140.
(12) Qin, J.; Wang, C.; Yao, Z.; Ma, Z.; Cui, X.; Gao, Q.; Wang, Y.; Wang, Q.; Wei, H. Influencing factors and growth kinetics analysis of carbon nanotube growth on the surface of continuous fibers. *Nanotechnology* **2021**, *32* (28), 285702.
(13) Zhu, J.; Jia, J.; Kwong, F.-l.; Ng, D. H. L. Synthesis of bamboo-like carbon nanotubes on a copper foil by catalytic chemical vapor deposition from ethanol. *Carbon* **2012**, *50* (7), 2504-2512.
(14) Lobo, L. S.; Carabineiro, S. A. Explaining bamboo-like carbon fiber growth mechanism: Catalyst shape adjustments above Tammann temperature. *C* **2020**, *6* (2), 18.
(15) Unalan, H. E.; Chhowalla, M. Investigation of single-walled carbon nanotube growth parameters using alcohol catalytic chemical vapour deposition. *Nanotechnology* **2005**, *16* (10), 2153.
(16) Ducati, C.; Alexandrou, I.; Chhowalla, M.; Robertson, J.; Amaratunga, G. The role of the catalytic particle in the growth of carbon nanotubes by plasma enhanced chemical vapor deposition. *J. Appl. Phys.* **2004**, *95* (11), 6387-6391.
(17) Kazakova, M. A.; Selyutin, A. G.; Semikolenova, N. V.; Ishchenko, A. V.; Moseenkov, S. I.; Matsko, M. A.; Zakharov, V. A.; Kuznetsov, V. L. Structure of the in situ produced polyethylene based composites modified with multi-walled carbon nanotubes: In situ synchrotron X-ray diffraction and differential scanning calorimetry study. *Compos. Sci. Technol.* **2018**, *167*, 148-154.

(18) Gili, A.; Schlicker, L.; Bekheet, M. F.; Görke, O.; Kober, D.; Simon, U.; Littlewood, P.; Schomäcker, R.; Doran, A.; Gaissmaier, D. Revealing the mechanism of multiwalled carbon nanotube growth on supported nickel nanoparticles by in situ synchrotron X-ray diffraction, density functional theory, and molecular dynamics simulations. *ACS Catal.* **2019**, *9* (8), 6999-7011.
(19) Rinaldi, A.; Tessonnier, J. P.; Schuster, M. E.; Blume, R.; Girgsdies, F.; Zhang, Q.; Jacob, T.; Abd Hamid, S. B.; Su, D. S.; Schlögl, R. Dissolved carbon controls the initial stages of nanocarbon growth. *Angew. Chem. Int. Ed.* **2011**, *50* (14), 3313-3317.
(20) Wirth, C.; Hofmann, S.; Robertson, J. State of the catalyst during carbon nanotube growth. *Diamond Relat. Mater.* **2009**, *18* (5-8), 940-945.
(21) Mattevi, C.; Hofmann, S.; Cantoro, M.; Ferrari, A.; Robertson, J.; Castellarin-Cudia, C.; Dolafi, S.; Goldoni, A.; Cepek, C. Surface-bound chemical vapour deposition of carbon nanotubes: In situ study of catalyst activation. *Phys. E* **2008**, *40* (7), 2238-2242.
(22) Rao, R.; Pierce, N.; Liptak, D.; Hooper, D.; Sargent, G.; Semiatin, S. L.; Curtarolo, S.; Harutyunyan, A. R.; Maruyama, B. Revealing the impact of catalyst phase transition on carbon nanotube growth by in situ Raman spectroscopy. *ACS nano* **2013**, *7* (2), 1100-1107.
(23) Rao, R.; Liptak, D.; Cherukuri, T.; Yakobson, B. I.; Maruyama, B. In situ evidence for chirality-dependent growth rates of individual carbon nanotubes. *Nat. Mater.* **2012**, *11* (3), 213-216.
(24) Picher, M.; Anglaret, E.; Jourdain, V. High temperature activation and deactivation of single-walled carbon nanotube growth investigated by in situ Raman measurements. *Diamond Relat. Mater.* **2010**, *19* (5-6), 581-585.
(25) Jinschek, J. Advances in the environmental transmission electron microscope (ETEM) for nanoscale in situ studies of gas–solid interactions. *Chem. Commun.* **2014**, *50* (21), 2696-2706.
(26) Tao, F.; Salmeron, M. In situ studies of chemistry and structure of materials in reactive environments. *Science* **2011**, *331* (6014), 171-174.
(27) Huang, X.; Farra, R.; Schlögl, R.; Willinger, M.-G. Growth and termination dynamics of multiwalled carbon nanotubes at near ambient pressure: an in situ transmission electron microscopy study. *Nano Lett.* **2019**, *19* (8), 5380-5387.
(28) Wang, Y.; Qiu, L.; Zhang, L.; Tang, D.-M.; Ma, R.; Wang, Y.; Zhang, B.; Ding, F.; Liu, C.; Cheng, H.-M. Precise identification of the active phase of cobalt catalyst for carbon nanotube growth by in situ transmission electron microscopy. *ACS nano* **2020**, *14* (12), 16823-16831.
(29) Fan, H.; Qiu, L.; Fedorov, A.; Willinger, M.-G.; Ding, F.; Huang, X. Dynamic State and active structure of Ni–Co catalyst in carbon nanofiber growth revealed by in situ transmission electron microscopy. *ACS nano* **2021**, *15* (11), 17895-17906.
(30) Ding, L.; Tselev, A.; Wang, J.; Yuan, D.; Chu, H.; McNicholas, T. P.; Li, Y.; Liu, J. Selective growth of well-aligned semiconducting single-walled carbon nanotubes. *Nano Lett.* **2009**, *9* (2), 800-805.
(31) Unocic, K. A.; Dagle, V. L.; Dagle, R. A.; Wegener, E. C.; Kropf, J.; Krause, T. R.; Ruddy, D. A.; Allard, L. F.; Habas, S. E. In situ S/TEM Reactions of Ag/ZrO2/SBA-16 Catalysts for Single-Step Conversion of Ethanol to Butadiene. *Microsc. Microanal.* **2019**, *25* (S2), 1460-1461.
(32) Yoshida, H.; Uchiyama, T.; Takeda, S. Direct observation of carbon nanotube growth by environmental transmission electron microscopy. In *Microscopy of Semiconducting Materials 2007*, 2008; Springer: pp 209-212.
(33) Zhang, F.; Pen, M.; Spruit, R. G.; Garza, H. P.; Liu, W.; Zhou, D. Data synchronization in operando gas and heating TEM. *Ultramicroscopy* **2022**, *238*, 113549.

(34) Takagi, D.; Homma, Y.; Hibino, H.; Suzuki, S.; Kobayashi, Y. Single-walled carbon nanotube growth from highly activated metal nanoparticles. *Nano Lett.* **2006**, *6* (12), 2642-2645.
(35) Helveg, S.; Lopez-Cartes, C.; Sehested, J.; Hansen, P. L.; Clausen, B. S.; Rostrup-Nielsen, J. R.; Abild-Pedersen, F.; Nørskov, J. K. Atomic-scale imaging of carbon nanofibre growth. *Nature* **2004**, *427* (6973), 426-429.
(36) Saito, Y. Nanoparticles and filled nanocapsules. *Carbon* **1995**, *33* (7), 979-988.
(37) Lisi, N.; Buonocore, F.; Dikonimos, T.; Leoni, E.; Faggio, G.; Messina, G.; Morandi, V.; Ortolani, L.; Capasso, A. Rapid and highly efficient growth of graphene on copper by chemical vapor deposition of ethanol. *Thin Solid Films* **2014**, *571*, 139-144.
(38) Faggio, G.; Capasso, A.; Messina, G.; Santangelo, S.; Dikonimos, T.; Gagliardi, S.; Giorgi, R.; Morandi, V.; Ortolani, L.; Lisi, N. High-temperature growth of graphene films on copper foils by ethanol chemical vapor deposition. *J. Phys. Chem. C* **2013**, *117* (41), 21569-21576.
(39) Guermoune, A.; Chari, T.; Popescu, F.; Sabri, S. S.; Guillemette, J.; Skulason, H. S.; Szkopek, T.; Siaj, M. Chemical vapor deposition synthesis of graphene on copper with methanol, ethanol, and propanol precursors. *Carbon* **2011**, *49* (13), 4204-4210.
(40) Peng, X.; Koczkur, K.; Chen, A. Synthesis of well-aligned bamboo-like carbon nanotube arrays from ethanol and acetone. *J. Phys. D: Appl. Phys.* **2008**, *41* (9), 095409.
(41) Maruyama, S.; Kojima, R.; Miyauchi, Y.; Chiashi, S.; Kohno, M. Low-temperature synthesis of high-purity single-walled carbon nanotubes from alcohol. *Chem. Phys. Lett.* **2002**, *360* (3-4), 229-234.
(42) Lyu, Y.; Wang, P.; Liu, D.; Zhang, F.; Senftle, T. P.; Zhang, G.; Zhang, Z.; Wang, J.; Liu, W. Tracing the active phase and dynamics for carbon nanofiber growth on nickel catalyst using environmental transmission electron microscopy. *Small Methods* **2022**, *6* (6), 2200235.
(43) Peng, Z.; Somodi, F.; Helveg, S.; Kisielowski, C.; Specht, P.; Bell, A. T. High-resolution in situ and ex situ TEM studies on graphene formation and growth on Pt nanoparticles. *J. Catal.* **2012**, *286*, 22-29.
(44) Hofmann, S.; Ducati, C.; Robertson, J.; Kleinsorge, B. Low-temperature growth of carbon nanotubes by plasma-enhanced chemical vapor deposition. *Appl. Phys. Lett.* **2003**, *83* (1), 135-137.
(45) Lobo, L. S.; Carabineiro, S. A. Kinetics of carbon nanotubes and graphene growth on iron and steel: evidencing the mechanisms of carbon formation. *Nanomaterials* **2021**, *11* (1), 143.
(46) Barrer, R. M. *Diffusion in and through Solids*; Рипол Классик, 1941.
(47) Furlan, A.; Lu, J.; Hultman, L.; Jansson, U.; Magnuson, M. Crystallization characteristics and chemical bonding properties of nickel carbide thin film nanocomposites. *J. Phys.: Condens. Matter* **2014**, *26* (41), 415501.
(48) Hwang, J.-W. Thermal expansion of nickel and iron, and the influence of nitrogen on the lattice parameter of iron at the Curie temperature. Missouri University of Science and Technology, 1972.
(49) Owen, E.; Yates, E. LXVI. X-ray measurement of the thermal expansion of pure nickel. *Philos. Mag. (1798-1977)* **1936**, *21* (142), 809-819.
(50) Singleton, M.; Nash, P. The C-Ni (carbon-nickel) system. *Bull. Alloy Phase Diagrams* **1989**, *10* (2), 121-126.
(51) Natesan, K.; Kassner, T. Thermodynamics of carbon in nickel, iron-nickel and iron-chromium-nickel alloys. *Metall. Trans.* **1973**, *4*, 2557-2566.
(52) Weatherup, R. S.; Amara, H.; Blume, R.; Dlubak, B.; Bayer, B. C.; Diarra, M.; Bahri, M.; Cabrero-Vilatela, A.; Caneva, S.; Kidambi, P. R. Interdependency of subsurface carbon distribution and graphene–catalyst interaction. *J. Am. Chem. Soc.* **2014**, *136* (39), 13698-13708.

(53) Piao, Y.; Meany, B.; Powell, L. R.; Valley, N.; Kwon, H.; Schatz, G. C.; Wang, Y. Brightening of carbon nanotube photoluminescence through the incorporation of sp 3 defects. *Nat. Chem.* **2013**, *5* (10), 840-845.
(54) Zheng, W.; Zorn, N. F.; Bonn, M.; Zaumseil, J.; Wang, H. I. Probing Carrier Dynamics in sp 3-Functionalized Single-Walled Carbon Nanotubes with Time-Resolved Terahertz Spectroscopy. *ACS nano* **2022**, *16* (6), 9401-9409.
(55) Zhang, Z.-l.; Brydson, R.; Aslam, Z.; Reddy, S.; Brown, A.; Westwood, A.; Rand, B. Investigating the structure of non-graphitising carbons using electron energy loss spectroscopy in the transmission electron microscope. *Carbon* **2011**, *49* (15), 5049-5063.
(56) Papworth, A.; Kiely, C.; Burden, A.; Silva, S.; Amaratunga, G. Electron-energy-loss spectroscopy characterization of the sp 2 bonding fraction within carbon thin films. *Phys. Rev. B* **2000**, *62* (19), 12628.
(57) Berger, S.; McKenzie, D.; Martin, P. EELS analysis of vacuum arc-deposited diamond-like films. *Philos. Mag. Lett.* **1988**, *57* (6), 285-290.
(58) Mironov, B.; Freeman, H.; Brown, A.; Hage, F.; Scott, A.; Westwood, A.; Da Costa, J.-P.; Weisbecker, P.; Brydson, R. Electron irradiation of nuclear graphite studied by transmission electron microscopy and electron energy loss spectroscopy. *Carbon* **2015**, *83*, 106-117.
(59) Smith, M.; Scudiero, L.; Espinal, J.; McEwen, J.-S.; Garcia-Perez, M. Improving the deconvolution and interpretation of XPS spectra from chars by ab initio calculations. *Carbon* **2016**, *110*, 155-171.
(60) Lesiak, B.; Kövér, L.; Tóth, J.; Zemek, J.; Jiricek, P.; Kromka, A.; Rangam, N. C sp2/sp3 hybridisations in carbon nanomaterials–XPS and (X) AES study. *Appl. Surf. Sci.* **2018**, *452*, 223-231.
(61) Zhu, Y.; Murali, S.; Stoller, M. D.; Ganesh, K. J.; Cai, W.; Ferreira, P. J.; Pirkle, A.; Wallace, R. M.; Cychosz, K. A.; Thommes, M. Carbon-based supercapacitors produced by activation of graphene. *science* **2011**, *332* (6037), 1537-1541.
(62) Haerle, R.; Riedo, E.; Pasquarello, A.; Baldereschi, A. sp 2/s p 3 hybridization ratio in amorphous carbon from C 1 s core-level shifts: X-ray photoelectron spectroscopy and first-principles calculation. *Phys. Rev. B* **2001**, *65* (4), 045101.
(63) Lajaunie, L.; Pardanaud, C.; Martin, C.; Puech, P.; Hu, C.; Biggs, M.; Arenal, R. Advanced spectroscopic analyses on a: CH materials: Revisiting the EELS characterization and its coupling with multi-wavelength Raman spectroscopy. *Carbon* **2017**, *112*, 149-161.
(64) Bokobza, L.; Bruneel, J.-L.; Couzi, M. Raman spectra of carbon-based materials (from graphite to carbon black) and of some silicone composites. *C* **2015**, *1* (1), 77-94.
(65) Santangelo, S.; Messina, G.; Faggio, G.; Lanza, M.; Milone, C. Evaluation of crystalline perfection degree of multi-walled carbon nanotubes: correlations between thermal kinetic analysis and micro-Raman spectroscopy. *J. Raman Spectrosc.* **2011**, *42* (4), 593-602.
(66) Osswald, S.; Flahaut, E.; Ye, H.; Gogotsi, Y. Elimination of D-band in Raman spectra of double-wall carbon nanotubes by oxidation. *Chem. Phys. Lett.* **2005**, *402* (4-6), 422-427.
(67) Li, H.; Yue, K.; Lian, Z.; Zhan, Y.; Zhou, L.; Zhang, S.; Shi, Z.; Gu, Z.; Liu, B.; Yang, R. Temperature dependence of the Raman spectra of single-wall carbon nanotubes. *Appl. Phys. Lett.* **2000**, *76* (15), 2053-2055.
(68) Sadezky, A.; Muckenhuber, H.; Grothe, H.; Niessner, R.; Pöschl, U. Raman microspectroscopy of soot and related carbonaceous materials: Spectral analysis and structural information. *Carbon* **2005**, *43* (8), 1731-1742.

(69) Vollebregt, S.; Ishihara, R.; Tichelaar, F.; Hou, Y.; Beenakker, C. Influence of the growth temperature on the first and second-order Raman band ratios and widths of carbon nanotubes and fibers. *Carbon* **2012**, *50* (10), 3542-3554.
(70) FC, T.; SL, T. Correlation between ID⁄ IG ratio from visible raman spectra and sp2/sp3 ratio from XPS spectra of annealed hydrogenated DLC film. *Mater. Trans.* **2006**, *47* (7), 1847-1852.
(71) Ferrari, A. C.; Robertson, J. Interpretation of Raman spectra of disordered and amorphous carbon. *Phys. Rev. B* **2000**, *61* (20), 14095.
(72) Jacobson, P.; Stöger, B.; Garhofer, A.; Parkinson, G. S.; Schmid, M.; Caudillo, R.; Mittendorfer, F.; Redinger, J.; Diebold, U. Disorder and defect healing in graphene on Ni (111). *J. Phys. Chem. Lett.* **2012**, *3* (1), 136-139.
(73) Li, J.; Croiset, E.; Ricardez-Sandoval, L. Carbon nanotube growth: First-principles-based kinetic Monte Carlo model. *J. Catal.* **2015**, *326*, 15-25.
(74) Wirth, C. T.; Zhang, C.; Zhong, G.; Hofmann, S.; Robertson, J. Diffusion-and reaction-limited growth of carbon nanotube forests. *ACS nano* **2009**, *3* (11), 3560-3566.
(75) Bartsch, K.; Biedermann, K.; Gemming, T.; Leonhardt, A. On the diffusion-controlled growth of multiwalled carbon nanotubes. *J. Appl. Phys.* **2005**, *97* (11), 114301.
(76) Lee, C. J.; Lyu, S. C.; Cho, Y. R.; Lee, J. H.; Cho, K. I. Diameter-controlled growth of carbon nanotubes using thermal chemical vapor deposition. *Chem. Phys. Lett.* **2001**, *341* (3-4), 245-249.
(77) Zhu, Y.-A.; Dai, Y.-C.; Chen, D.; Yuan, W.-K. First-principles study of C chemisorption and diffusion on the surface and in the subsurfaces of Ni (1 1 1) during the growth of carbon nanofibers. *Surf. Sci.* **2007**, *601* (5), 1319-1325.
(78) Shibuta, Y.; Maruyama, S. A molecular dynamics study of the effect of a substrate on catalytic metal clusters in nucleation process of single-walled carbon nanotubes. *Chem. Phys. Lett.* **2007**, *437* (4-6), 218-223.